J. Fluid Mech. (2002), *vol.* 471, *pp.* 381–408. © 2002 Cambridge University Press
DOI: 10.1017/S0022112002002240 Printed in the United Kingdom

Large-scale dynamics in turbulent mixing and the three-dimensional space–time behaviour of outer fluid interfaces

By HARIS J. CATRAKIS, ROBERTO C. AGUIRRE, JESUS RUIZ-PLANCARTE, ROBERT D. THAYNE, BRENDA A. McDONALD AND JOSHUA W. HEARN

Aeronautics and Fluid Dynamics Laboratories, University of California, Irvine, CA 92697, USA

(Received 4 February 2002 and in revised form 22 May 2002)

Experiments have been conducted to investigate turbulent mixing and the dynamics of outer fluid interfaces, i.e. the interfaces between mixed fluid and pure ambient fluid. A novel six-foot-diameter octagonal-tank flow facility was developed to enable the optical imaging of fluid interfaces above the mixing transition, corresponding to fully developed turbulence. Approximately 1000^3 whole-field three-dimensional space–time measurements of the concentration field were recorded using laser-induced-fluorescence digital-imaging techniques in turbulent jets at a Reynolds number of $Re \sim 20\,000$, Schmidt number of $Sc \sim 2000$, and downstream distance of ~ 500 nozzle diameters. Multiple large-scale regions of spatially nearly uniform-concentration fluid are evident in instantaneous visualizations, in agreement with previous findings above the mixing transition. The ensemble-averaged probability density function of concentration is found to exhibit linear dependence over a wide range of concentration thresholds. This can be accounted for in terms of the dynamics of large-scale well-mixed regions. Visualization of the three-dimensional space–time concentration field indicates that molecular mixing of entrained pure ambient fluid is dynamically initiated and accomplished in the vicinity of the unsteady large scales. Examination of the outer interfaces shows that they are dynamically confined primarily near the instantaneous large-scale boundaries of the flow. This behaviour is quantified in terms of the probability density of the location of the outer interfaces relative to the flow centreline and the probability of pure ambient fluid as a function of distance from the centreline. The current measurements show that the dynamics of outer interfaces above the mixing transition is significantly different from the behaviour below the transition, where previous studies have shown that unmixed ambient fluid can extend across a wide range of transverse locations in the flow interior. The present observations of dynamical confinement of the outer interfaces to the unsteady large scales, and considerations of entrainment, suggest that the mechanism responsible for this behaviour must be the coupling of large-scale flow dynamics with the presence of small-scale structures internal to the large-scale structures, above the mixing transition. The dynamics and structure of the outer interfaces across the entire range of space–time scales are quantified in terms of a distribution of generalized level-crossing scales. The outer-interface behaviour determines the mixing efficiency of the flow, i.e. fraction of mixed fluid. The present findings indicate that the large-scale dynamics of the outer interfaces above the mixing transition provides the dominant contribution to the mixing efficiency. This suggests a new way to quantify the mixing efficiency of turbulent flows at high Reynolds numbers.

1. Introduction

Turbulent fluid interfaces such as concentration, density or vorticity interfaces are observed to exhibit dynamics across a wide range of scales at high Reynolds numbers (e.g. Brown & Roshko 1974; Roshko 1976; Liepmann 1979; Dimotakis, Miake-Lye & Papantoniou 1983; Sreenivasan 1991; Smits & Dussauge 1996; Adrian, Meinhart & Tomkins 2000). Fundamental and practical aspects of the behaviour of fluid interfaces, such as their dynamics, structure, and dependence on Reynolds number, Mach number, Schmidt number, inflow/outflow conditions, flow scale and other fluid/flow parameters, are subjects of ongoing studies (e.g. Sreenivasan & Meneveau 1986; Pope 1988; Prasad & Sreenivasan 1990; Sreenivasan 1991; Vassilicos & Hunt 1991; Lane-Serff 1993; Yoda, Hesselink & Mungal 1994; Catrakis & Dimotakis 1996*a*, 1998; Smits & Dussauge 1996; Frederiksen, Dahm & Dowling 1997; Dalziel, Linden & Youngs 1999; Villermaux & Innocenti 1999). Fluid interfaces correspond to surfaces in the flow associated with a given fluid or flow property, e.g. isoconcentration surfaces in turbulent mixing or isodensity surfaces in compressible turbulence. Knowledge of the dynamics of the interfaces is particularly important for physically based descriptions, predictions, and control in applications such as mixing (e.g. Catrakis, Aguirre & Ruiz-Plancarte 2002) and aerooptics (e.g. Dimotakis, Catrakis & Fourguette 2001) at high Reynolds numbers.

The dynamics of the interfaces across the entire range of scales needs to be understood. The large-scale interfacial behaviour and entrainment, for example, constrain the total amount of mixing possible for given flow conditions (e.g. Dimotakis 1991). The large scales are known to be particularly amenable to flow control (e.g. Gad-el-Hak 2000). The small-scale behaviour is also significant because it can dominate the total area–volume ratio of the interfaces (e.g. Catrakis *et al.* 2002). Knowledge of the dynamics and structure of mixed-fluid interfaces across the entire range of interfacial scales can be expected to facilitate the development of predictive frameworks of the mixing efficiency in turbulent flows. The large-scale dynamics of fluid interfaces in high-Reynolds-number turbulent flows can provide the basis for developing predictive descriptions useful in various applications. In aero-optics, for example, the signature of optical beams propagating through turbulent incompressible or compressible flows is intimately related to the behaviour of the turbulent refractive fluid interfaces. Knowledge of the instantaneous behaviour of such interfaces is essential for prediction and control of aero-optical interactions (e.g. Jumper & Fitzgerald 2001) as has been demonstrated, for example, in optical beam propagation through high-Reynolds-number incompressible turbulent shear layers (Dimotakis *et al.* 2001). The outer interfaces, or interfaces between mixed fluid and pure ambient fluid, can provide the dominant large-scale contributions to the distortion of aero-optical wavefronts. More generally, the outer interfaces reflect the mechanism by which turbulent mixing of pure ambient fluid is initiated dynamically in the flow.

In both free-shear and wall-bounded turbulent flows there is evidence of significant qualitative changes in mixing, and consequently in the behaviour of the fluid interfaces, across the mixing transition (e.g. Roshko 1991; Dimotakis 2000; and references therein). This transition is physically equivalent to the transition to fully developed turbulence, with the term mixing transition emphasizing the change in mixing behaviour observed for flows of miscible fluids. Various experimental observations and theoretical arguments indicate that the large-scale Reynolds number must be at a minimum in the range $Re \sim 10\,000$–$20\,000$. Because the mixing behaviour can be qualitatively different across the transition, the important consequence is that measurements or numerical simulations above the mixing transition are essential to contribute toward the development of predictive descriptions of the flow behaviour and mixing dynamics in high-Reynolds-number turbulent flows, which are important fundamentally as well as practically.

The development of high-resolution flow-imaging techniques has made possible multi-dimensional measurements of fluid interfaces which are very helpful in examining the large-scale as well as small-scale properties. Optical imaging enables non-intrusive flow measurements which can be utilized to examine the interfacial behaviour above the mixing transition (e.g. Catrakis & Dimotakis 1996*a*). Two-dimensional spatial imaging of concentration fields has been conducted to study the spatial structure of mixed-fluid interfaces as a function of scale (e.g. Sreenivasan & Meneveau 1986; Lane-Serff 1993; Catrakis & Dimotakis 1996*a*; Villermaux & Innocenti 1999). Three-dimensional spatial imaging has been conducted to examine the instantaneous large-scale structure of concentration fields (Yoda *et al.* 1994). Experimental studies of properties of fluid interfaces at small scales, including an assessment of fractal scaling, have also been conducted (e.g. Prasad & Sreenivasan 1990; Frederiksen *et al.* 1997; Catrakis *et al.* 2002).

In the present study, the dynamics of mixing and of the outer fluid interfaces in fully developed turbulence are examined on the basis of whole-field three-dimensional space–time concentration measurements above the mixing transition. In § 2, the experimental procedure and imaging technique are described, including an overview of the octagonal-tank flow facility. In § 3, results are presented for the whole-field mixing behaviour on the basis of flow visualizations and the probability density function of the concentration field. In § 4, the dynamics of the outer interfaces are investigated on the basis of the three-dimensional space–time measurements and quantified in terms of the probability density of the location of the outer interfaces relative to the flow centreline and the probability of pure ambient fluid as a function of distance from the centreline. The relation between the outer-interface dynamics and the mixing efficiency of the flow is also examined. In § 5, the behaviour of the interfaces in space and time throughout the range of scales is quantified in terms of a distribution of generalized level-crossing scales. Mechanisms that account for the observed interfacial behaviour are discussed in §§ 3–5. Implications of the present findings for quantifying the dynamics of outer fluid interfaces and mixing in high-Reynolds-number turbulent flows in general are also discussed.

2. Experiments

The experiments were conducted in a novel flow facility housed in the Aeronautics and Fluid Dynamics Laboratories at UC Irvine. A large octagonal tank, shown in figure 1, was specifically designed and constructed to facilitate the optical imaging of fluid interfaces in turbulent flows above the mixing transition, by virtue of the size of the facility. The tank has an internal diameter of 6 ft and an internal height of 9 ft. It can be filled with 8 tons of filtered, softened, and deionized water prior to each experiment. Optical access is available through eight 2 ft × 7 ft optical-quality vertical windows and a 2 ft-diameter horizontal window centred at the bottom face of the tank. The choice of the octagonal cross-section of the tank, as opposed to a square cross-section for example, was made for several reasons. First, in studies of flows such as the round turbulent jet, this provides boundary conditions that are more appropriate than with a square tank. Secondly, the octagonal cross-section makes more efficient use of space and helps minimize the amount of water needed. Thirdly, the octagonal shape results in eight vertical windows as two sets of four orthogonally oriented windows that make possible laser-sheet propagation and optical imaging

FIGURE 1. Side view of the facility designed, constructed and operated for the present experiments that enabled $\sim 1000^3$ whole-field concentration measurements above the mixing transition. The octagonal tank provides four pairs of vertical windows at right angles to each other that facilitate non-intrusive optical imaging of the flow. The tank has an internal diameter of 6 ft, an internal height of 9 ft, and a capacity of 8 tons of water. A jet seeded with dilute aqueous disodium fluorescein dye was generated in a blow-down manner and issued through a nozzle of exit diameter $d = 2.54$ mm machined flush with the base plate of the plenum, visible at the top. The jet was directed downwards at a Reynolds number of $Re \sim 20\,000$ with a Schmidt number of $Sc \sim 2000$. Imaging was conducted in the far field of the flow at a downstream distance of $z/d \sim 500$ nozzle diameters and the large-scale transverse extent of the flow at the imaging location was $\delta \sim 0.5$ m.

normal to the optical-window surfaces. By virtue of its extensive optical access and large capacity, this flow facility provides a unique turbulence-visualization and flow-imaging environment that can be utilized to trade flow velocity for size. This enables the quantitative study of the behaviour of turbulent flows above the mixing transition in the controlled environment of the laboratory.

In the present experiments, the flow facility and imaging diagnostics were configured to record whole-field three-dimensional space–time measurements of concentration in the far field of round turbulent jets above the mixing transition. The facility was operated in a blow-down manner to generate a liquid-phase turbulent jet vertically downwards issued from a contoured sixth-order-polynomial machined aluminium nozzle of exit diameter $d = 2.54\,\mathrm{mm}$, with the nozzle exit machined flush with the base plate of the jet plenum. The jet velocity U_0 at the nozzle exit was $8\,\mathrm{m\,s^{-1}}$ and this resulted in a jet Reynolds number of $Re \sim 20\,000$ based on the nozzle diameter and the water viscosity $\nu \sim 10^{-6}\,\mathrm{m^2\,s^{-1}}$. The ratio of the internal diameter of the tank to the diameter of the nozzle was 720. The large size of the facility and the small nozzle exit diameter resulted in the capability to conduct measurements at a far-field downstream distance of $z/d \sim 500$, above the mixing transition, that captured the whole-field dynamics of the outer fluid interfaces. The turbulent jet provides a flow environment where the Reynolds number does not change with downstream distance, since the growth rate is linear and the mean centreline velocity is inversely proportional to downstream distance. The reduced flow velocities in the far field facilitate the imaging of the dynamics of the fluid interfaces by relaxing the temporal-resolution requirements. Also, the smallest spatial scales in the jet grow with increasing downstream distance. The capability to record far-field measurements in this flow, facilitated by the large tank size, therefore relaxes both the temporal and spatial resolution requirements.

The illumination source was a 6 W continuous-wave argon-ion laser (Coherent Innova 305) operated in the multiline-visible mode. The laser was operated in power-regulation mode to ensure stability of the laser-power output in the course of the experiments. The laser beam was directed through a long-focal-length $f = 2\,\mathrm{m}$ spherical bi-convex lens and a short-focal-length $f = -6.25\,\mathrm{mm}$ cylindrical plano-concave lens to generate a laser sheet of nominal waist thickness $\lambda_z \sim 500\,\mu\mathrm{m}$. The laser sheet was directed into the tank with the laser-sheet plane transverse to the jet axis, i.e. in the similarity plane of the flow, and measurements were acquired in this plane to capture the dynamics and structure of the interfaces. A 45° mirror was positioned below the tank and was employed to facilitate optical imaging through the 2 ft diameter window on the bottom face of the tank. The similarity plane for this flow will be denoted the (x, y)-plane, cf. the schematic in figure 2, with the z-axis taken as the jet axis, i.e. flow centreline. The origin of the (x, y)-plane is taken to be the intersection of the jet axis and the imaging plane. Investigating the behaviour of fluid interfaces in the similarity plane and in the far field of the flow has two important advantages. First, imaging at a constant downstream distance in the far field of the flow removes the streamwise dependence of the large scales of the flow. Secondly, the behaviour of the fluid interfaces in the similarity plane can be scaled in a simple manner using the jet linear growth-rate law to describe the behaviour at other far-field flow locations.

The jet was seeded with aqueous disodium fluorescein with Schmidt number $Sc \sim 2000$. The dye concentration was $c_0 \sim 7 \times 10^{-6}\,\mathrm{M}$ for a sufficient fluorescence signal at the downstream measurement location with negligible laser beam attenuation. The experiments were conducted in a temperature-controlled room in order to eliminate bouyancy effects. The plenum water temperature was measured to match the water temperature in the tank. Based on the precision of the water temperature measurements, it was estimated that the bouyancy length scale was at least four times the downstream measurement distance, thus resulting in a purely momentum-driven jet. All light sources in the laboratory, other than the laser, were turned off or covered to minimize noise. A sheet of neoprene, attached to the rear windows inside the tank,

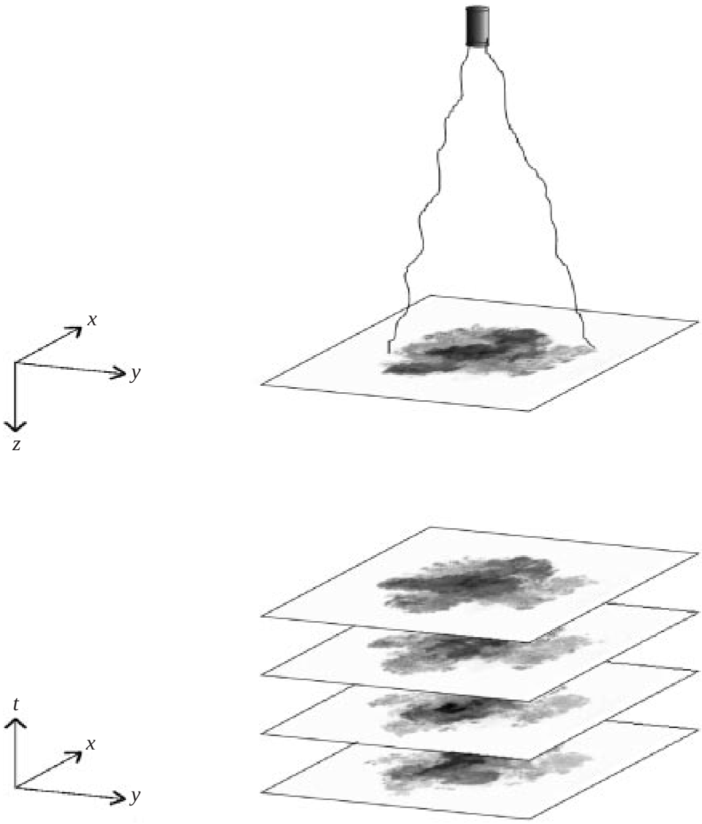

FIGURE 2. Schematic (not to scale) of the flow-imaging orientation employed in the present experiments, cf. figure 1. A laser sheet was propagated horizontally into the octagonal tank through one of the eight side windows to illuminate the far field of the flow. A 2 ft-diameter window centred at the bottom face of the tank and a 45° mirror positioned below the tank enabled imaging of the fluorescence-field intensity using a high-resolution digital camera operated continously in time to record data sets each of $\sim 1000^3$ three-dimensional space–time x, y, t concentration measurements. The x, y, t image-volume reconstruction was performed by stacking sequential two-dimensional spatial realizations of the concentration field in time, as indicated.

reduced reflections of the incident laser sheet. Before each run was conducted, the laser was turned on and maintained at full laser power for one hour to allow for power stability. Two hours prior to each run, a recirculating pump with a microfilter was employed to reduce the gas content in the water and minimize any scattering in the imaging due to gas bubbles. The tank water was left undisturbed for one hour before conducting each run.

At the imaging station, the large scale of the jet was $\delta \sim 0.5$ m and the mean velocity at the centreline was $U_{\mathrm{cl}} \sim 10\,\mathrm{cm\,s^{-1}}$. The jet large scale at the imaging station was less than a third of the internal diameter of the tank and the downstream distance from the nozzle to the imaging location was less than half the tank height. This resulted in negligible endwall and sidewall effects during the duration of each experiment. The ratio of the largest to the smallest concentration-field spatial or temporal scales was estimated to be 1000 : 1 on the jet centreline on the basis of Kolmogorov and Batchelor scaling, with the smallest scale here taken as the scale needed to resolve the knee of the energy spectrum roll-off as in previous studies (e.g. Catrakis & Dimotakis

1996*a*). The smallest spatial and temporal scales were estimated to be $\lambda_c \sim 500\,\mu\text{m}$ and $\tau_c \sim \lambda_c/U_{\text{cl}} \sim 5\,\text{ms}$ on the jet centreline and were larger away from the centreline where the focus of this study is. The dye fluorescence was collected with a 35 mm f/1.4 Nikon lens and recorded using a digital-imaging system based on a 1008×1018-pixel 10-bit CCD sensor (Kodak KAI-1010M) at a framing rate of 30 frames/s and an individual-image electronic-shutter exposure time of 20 ms. A total of 972 temporally sequential images were recorded per run, resulting in individual image-data volumes of $972 \times 1008 \times 1018 \sim 1000^3$ measurements each, or approximately 2 GB each, as two bytes per pixel were employed to store each 10-bit data value to memory in real time. The framing rate was selected to match the mean velocity of the outer interfaces. Each resulting $\sim 1000^3$ space–time data set corresponds to the passage of approximately three large structures, estimated in terms of the large-structure passage time $\tau_\delta = \delta/U_c \sim 10\,\text{s}$ and the large-structure velocity $U_c = U_{\text{cl}} - 0.5\Delta U \sim 5\,\text{cm}\,\text{s}^{-1}$, where ΔU is the shear which is $\Delta U = U_{\text{cl}}$ for the jet. In the outer and neighbouring internal regions of the flow at least, these measurements satisfy the Nyquist criterion in three space–time dimensions. Four runs were conducted at the same flow conditions, resulting in a total of $\sim 4 \times 10^9$ individual measurements, and were found to be adequate to evaluate statistics of the whole-field behaviour of the concentration field and fluid interfaces, such as the probability density function of concentration in § 3, the dynamics of the outer interfaces in § 4, and the distribution of interfacial scales in § 5.

The three-dimensional space–time data sets were processed to calibrate and normalize pixel-by-pixel each individual two-dimensional spatial fluorescence-intensity image for noise, sensitivity and laser illumination variations in the field of view. This was achieved by recording a set of ten background-noise images, prior to each run, and a set of ten uniform-concentration images, after each run. Both the pre-run background-noise images and the post-run uniform-concentration images were recorded physically in the same imaging plane in the tank as the flow images so that the optical path was identical for all three types of image. The background-noise images were recorded by directing the laser sheet into the tank in the same manner as for the jet imaging, but with pure water without dye in the tank. To generate the uniform-concentration field needed for the calibration and normalization images, all the water and dye in the tank were recirculated continuously after each run and the fluorescence at the imaging plane was monitored for a sufficiently long time, which was one hour for each of the present experiments, until intensity non-uniformities were no longer measurable. The resulting signal-to-noise ratio of the calibrated and normalized three-dimensional x, y, t image-volume measurements, estimated on the basis of concentration-field power spectra, was found to be comparable to the 300 : 1 signal-to-noise ratio of the two-dimensional spatial concentration-field images in Catrakis & Dimotakis (1996*a*). Care was taken to ensure that a known volume of water was employed each time to fill the tank and a known amount of dye was discharged into the tank during each run. This is important because it enabled the use of the post-run uniform-concentration images as reference images to measure the illumination and optical-collection efficiency field in the field of view as well as to provide absolute concentration measurements.

3. Whole-field mixing behaviour

The present three-dimensional space–time x, y, t measurements permit an examination of the whole-field mixing behaviour. Figures 3(*a*) and 3(*b*) depict examples of concentration-field visualizations. In figure 3(*a*), the visualization is normal to the time axis with time increasing vertically. A view along the time axis is depicted in figure 3(*b*). A transparent-visualization image-processing technique was employed to render features of the concentration field visible throughout the $\sim 1000^3$ data set shown in figure 3(*a, b*). In this way, the mixing behaviour corresponding to both early times and later times is visible in figure 3(*b*). Analogously, the flow dynamics over the entire range of transverse locations relative to the flow centreline is visible in figure 3(*a*). Large-scale dynamics of the concentration field are evident primarily in the interior of the flow. The spatial extent shown spans the largest transverse scale of the jet which, as noted in § 2, is physically $\delta \sim 0.5$ m. The dynamics corresponds to a continuous time period equivalent to the passage of approximately three large-scale structures, as discussed in § 2. In figure 3(*a*), the upper space–time regions correspond to upstream flow dynamics and the lower space–time regions correspond to downstream flow dynamics, since time increases from bottom to top in that visualization as noted above. Both figures 3(*a*) and 3(*b*) indicate that the mixed-fluid interfaces, or surfaces of constant concentration, are convoluted across the entire range of concentration values, at least on the basis of these whole-field visualizations. The present three-dimensional space–time measurements enable an examination of both the temporal dynamics and spatial structure of mixing and of the mixed-fluid interfaces. In this section, the mixing behaviour will be examined in terms of visualizations of the space–time dynamics of the concentration field and of its spatial structure. The whole-field mixing behaviour will be quantified in terms of the probability density of concentration corresponding to the x, y, t measurements.

A two-dimensional space–time x, t visualization of the concentration field in the vicinity of the flow centreline, derived from the present three-dimensional space–time x, y, t measurements, is shown in figure 4(*a*). The colours shown were chosen to aid the eye in visualizing the large-scale and small-scale extent of mixing, i.e. homogenization of the concentration field, as well as the dynamics of the fluid interfaces. Figure 4(*a*) suggests that pure ambient fluid, denoted by black in this visualization, is rarely found in the interior of the flow. Visual observation of the dynamics of the outer interface in figure 4(*a*), i.e. the interface between pure ambient fluid (black) and low-concentration fluid (blue), indicates that this interface is dynamically confined primarily near the instantaneous unsteady large-scale boundaries of the flow. The measurements in figure 4(*a*) also indicate that the low-concentration fluid (blue) is confined largely away from the flow centreline. These observations suggest that the dominant behaviour in the whole-field mixing dynamics, as far as mixing of pure ambient fluid is concerned, is that the ambient fluid is dynamically mixed in the vicinity of the instantaneous large scales of the flow: mixing of ambient fluid is initiated primarily in the unsteady outer regions of the flow. Numerous other two-dimensional space–time slices were derived from the present three-dimensional space–time data, in planes at random orientations in the vicinity of the flow centreline, and similar behaviour was observed regarding the mixing of pure ambient fluid.

An example of a two-dimensional spatial x, y image of the concentration field normal to the flow centreline, extracted from the three-dimensional space–time concentration-field data, is depicted in figure 4(*b*). This visualization also indicates that pure ambient fluid (black) is rarely present in the interior of the flow. Low-concentration fluid (blue) is observed to be spatially located mostly in the outer region of the flow. The spatial concentration field, in figure 4(*b*), indicates again that the interface between pure ambient fluid (black) and low-concentration fluid (blue) is dynamically confined primarily near the instantaneous large scales. This behaviour was confirmed in numerous other spatial x, y images derived from the present

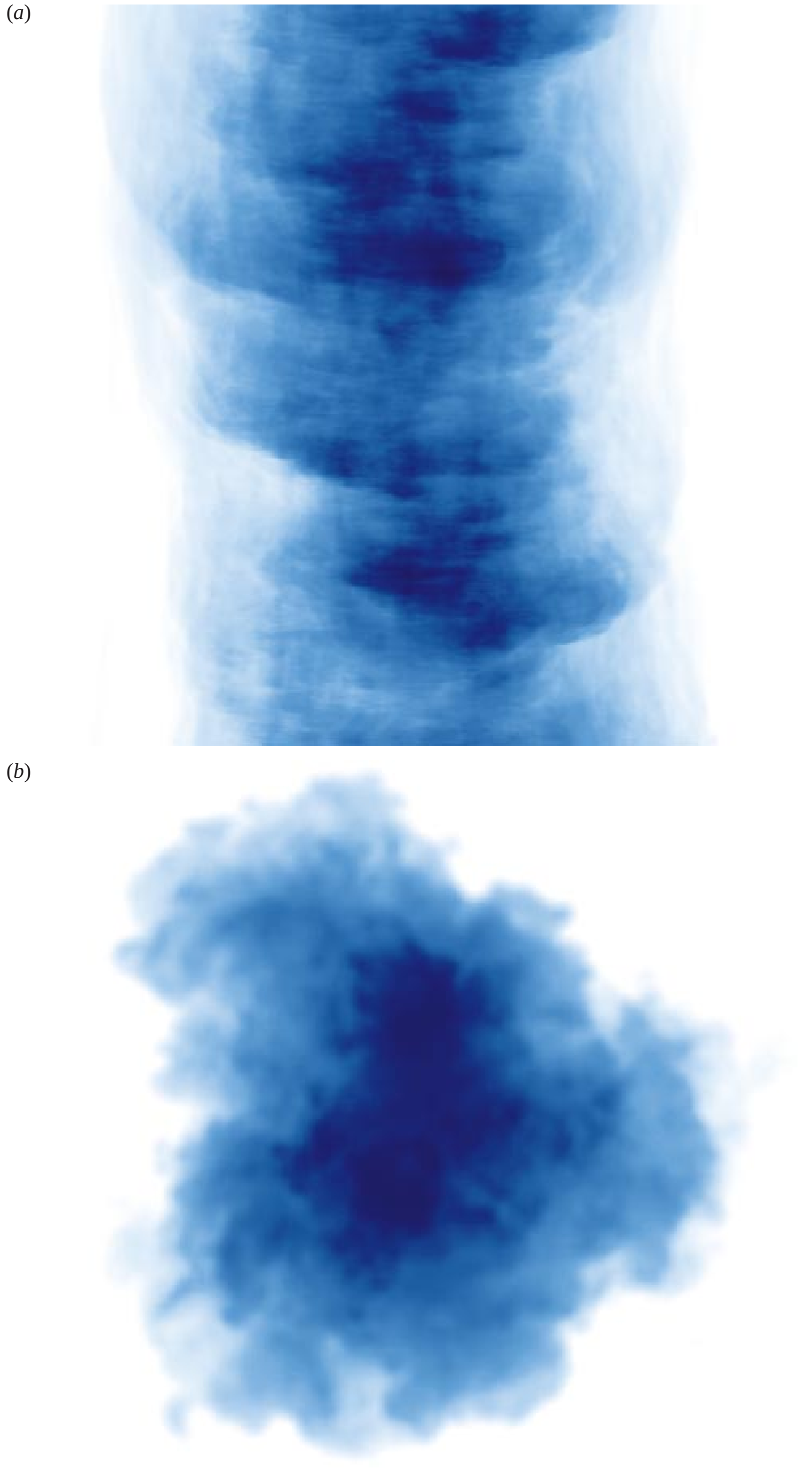

FIGURE 3. Transparent visualizations of the whole-field $\sim 1000^3$ three-dimensional space–time x, y, t measurements, cf. figure 2. Blue colours label the concentration field with darker shades denoting higher concentration. White corresponds to pure ambient fluid. (*a*) View normal to the time axis with time increasing vertically; (*b*) view along the time axis.

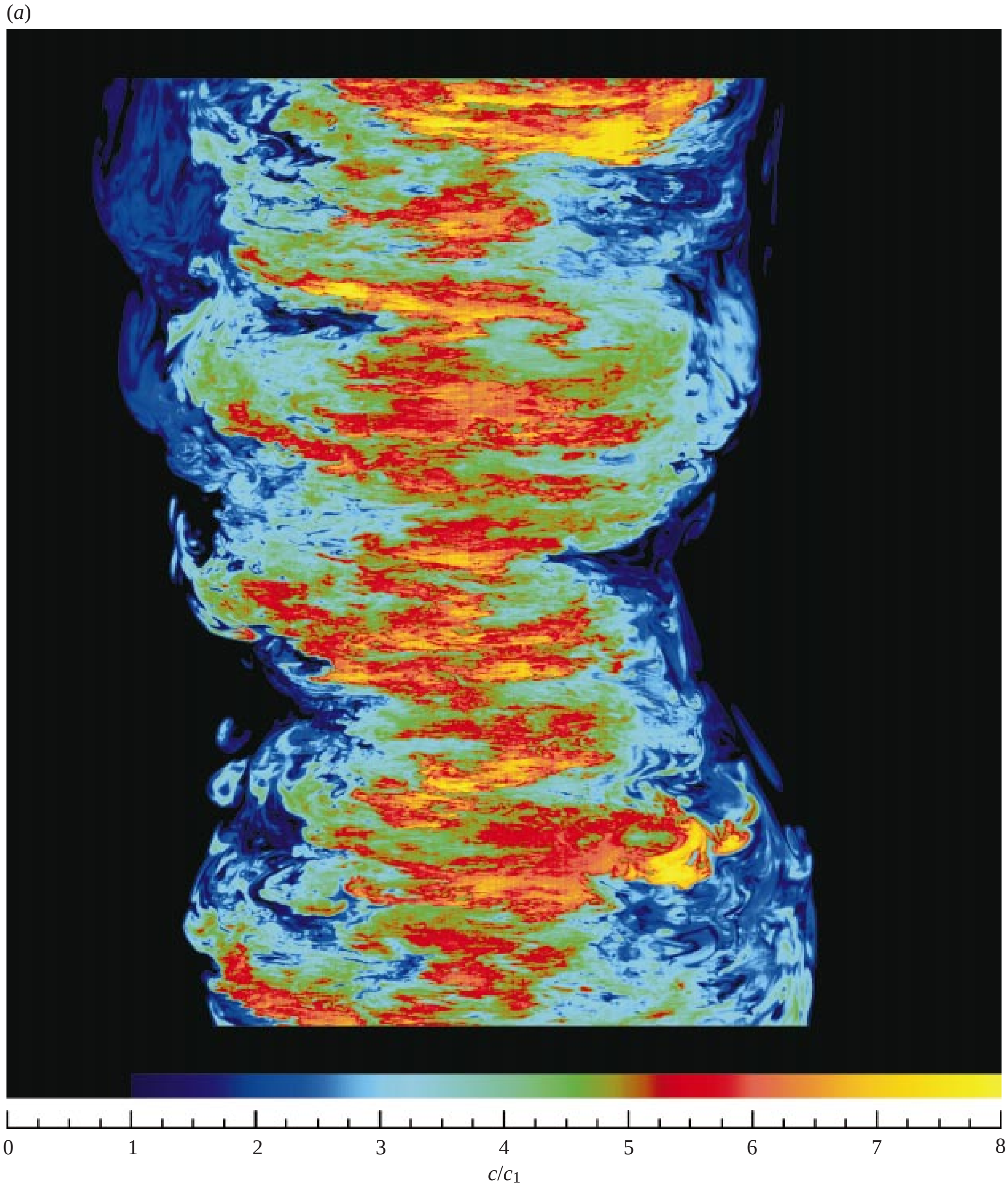

FIGURE 4 (*a*). For caption see facing page.

measurements and supports the above observation, i.e. that molecular mixing of entrained pure ambient fluid is initiated and accomplished mostly in the instantaneous outer-scale regions of the flow.

The present observations indicate that the dynamics of mixing, above the mixing transition, is significantly different when compared to the known behaviour below the transition, cf. discussion in § 1. Various studies conducted in the past have shown that, below the transition, pure ambient fluid is able to penetrate, and remain unmixed, deep into the interior of the flow, often crossing the flow centreline (e.g. Dimotakis *et al.* 1983; Dahm & Dimotakis 1990; Catrakis & Dimotakis 1996*a*, figure 3). Above the transition, the present data indicate that the behaviour of the concentration

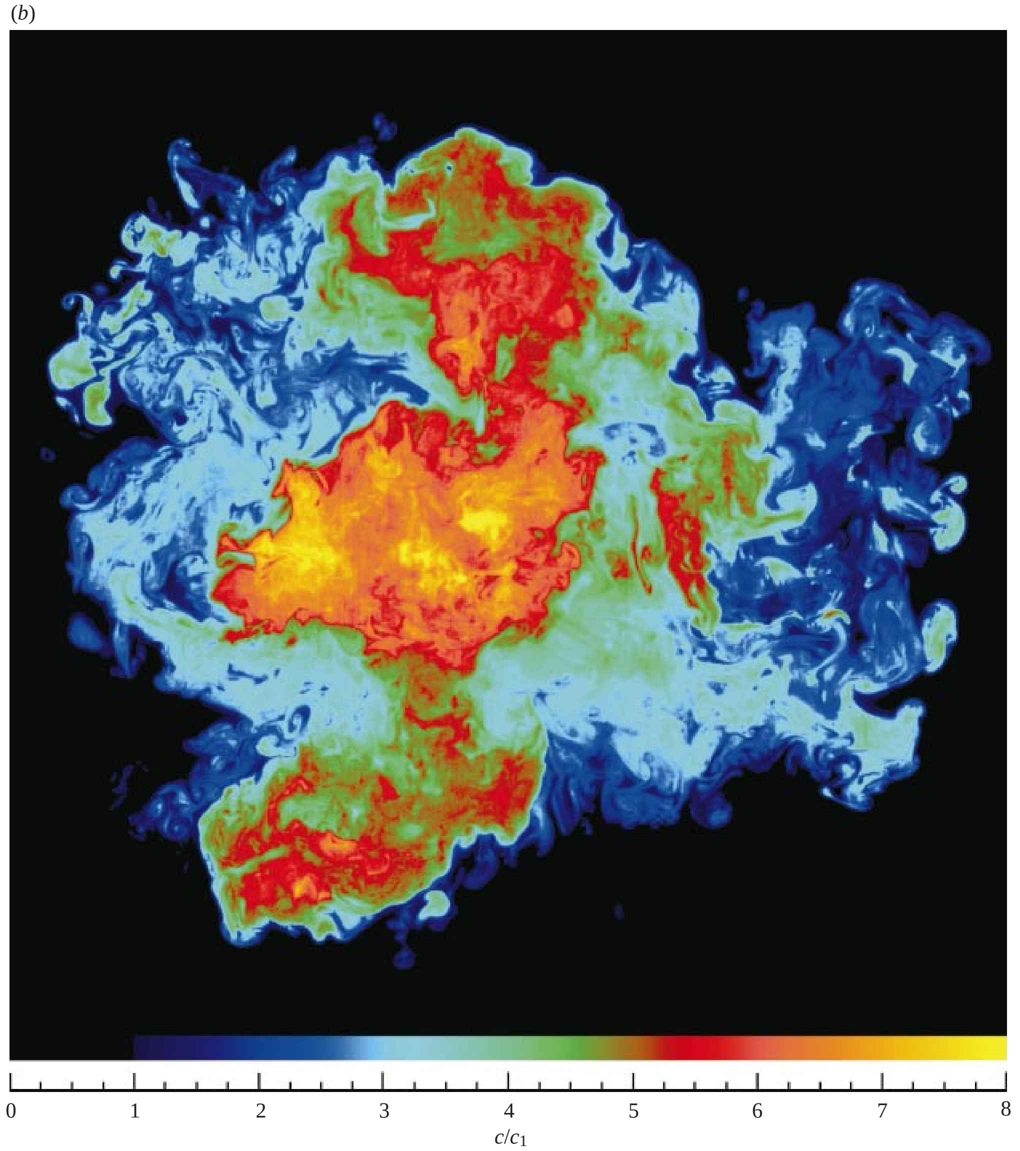

FIGURE 4. (*a*) An example of a two-dimensional space–time x, t concentration-field image, in the vicinity of the flow centreline, derived from the present three-dimensional space–time x, y, t measurements, cf. figure 3(*a*). Time increases vertically. Flow dynamics upstream and downstream correspond to the upper and lower regions respectively. This visualization depicts the dynamics and structure of the concentration field as well as of the mixed-fluid interfaces. The colours label concentration values and were applied to aid the eye in visualizing the global as well as local extent of mixing and the behaviour of the fluid interfaces. Pure ambient fluid is denoted by black. Low-concentration mixed fluid is denoted by blue. These measurements indicate that pure ambient fluid (black) is rarely present in the interior of the flow. The outer interface, i.e. the blue/black interface between mixed fluid and pure ambient fluid, appears to be dynamically confined primarily near the instantaneous large-scale boundaries of the flow, suggesting that mixing of pure ambient fluid is initiated predominantly in those regions. Numerous other two-dimensional space–time images near the flow centreline and at random orientations were visualized from the x, y, t data and were found to exhibit similar behaviour. (*b*) An example of a two-dimensional spatial x, y concentration-field image derived from the present three-dimensional space–time x, y, t measurements, cf. figure 3(*b*). This visualization is a view normal to the flow centreline and the colours label the concentration values. Pure ambient fluid (black) is rarely found in the interior of the flow, again indicating that mixing is initiated near the large scales of the flow. Large-scale regions of well-mixed fluid are evident.

field is markedly different. Mixing of pure ambient fluid is accomplished primarily prior to penetrating the interior of the flow, cf. figures 4(*a*) and 4(*b*). It may be noted, in the context of two-dimensional spatial or space–time concentration-field images alone, that a single two-dimensional image below the transition showing pure ambient fluid remaining unmixed deep in the interior of the flow is sufficient to conclude that pure ambient fluid can become mixed deep in the flow interior below the transition. In contrast, above the transition, two-dimensional spatial data (e.g. Catrakis & Dimotakis 1996*a*), or point measurements on the flow centreline (e.g. Dahm & Dimotakis 1990), or two-dimensional space–time data, cannot be expected to be sufficient to conclude whether or not mixing is dynamically initiated in the vicinity of the large scales. Whole-field three-dimensional space–time concentration measurements, as in this study, are crucial above the transition to examine directly the large-scale dynamics of the outer interfaces and to identify the mechanism by which molecular mixing of pure ambient fluid is initiated and its relation to the instantaneous large scales of the flow.

In the context of the mixing efficiency of the flow, i.e. the fraction of mixed fluid, the present observations are consistent with enhanced mixing across the transition: since the flow interior is occupied primarily by mixed fluid above the transition, as shown in figure 4(*a, b*), a larger mixing efficiency can be expected when compared to the behaviour below the transition for which a larger fraction of unmixed fluid is observed in the flow interior (cf. Catrakis & Dimotakis 1996*a*, figure 3). The present findings indicate that this mixing enhancement is associated with the flow dynamically initiating mixing of pure ambient fluid in the vicinity of the unsteady large-scale boundaries. In this way, ambient fluid penetrates the interior of the flow primarily as mixed fluid. This behaviour will be interpreted further by examining the dynamics of the outer interfaces in § 4.

The concentration-field probability density function, $p(c)$, can be examined and interpreted in terms of the behaviour of the mixed-fluid interfaces. Specifically, the probability density of concentration can be expressed in terms of the volume fraction of fluid internal to the interfaces,

$$p(c) \equiv \frac{1}{V_\delta}\left|\frac{\mathrm{d}V(c)}{\mathrm{d}c}\right|, \quad \text{with} \quad \int_0^{c_0} p(c)\,\mathrm{d}c = 1, \tag{3.1}$$

where $V(c)$ is the volume contained inside the c-threshold fluid interfaces, for $c_1 \leqslant c \leqslant c_0$, and corresponds to fluid with concentration values larger than or equal to c, cf. figure 4(*a, b*). The normalizing volume V_δ corresponds to the maximum large-scale boundaries of the flow. The individual probability density function, or distribution, was computed first for each three-dimensional space–time concentration data set, and then the ensemble average of these distributions was computed to determine $p(c)$, shown in figure 5(*a*). The measurements indicate that the concentration-field probability density exhibits linear behaviour over a wide range of thresholds in the interior of the flow. This finding is important because it provides a means to predict mixing at high Reynolds numbers above the mixing transition. It can be interpreted in terms of the dynamics of large-scale well-mixed regions in the flow as will be examined below.

The $c = c_1$ threshold, as indicated in figure 5(*a*), is in the vicinity of the local minimum of the concentration-field probability density function and corresponds to the outer interfaces. It will be utilized in § 4 to study the dynamics of these interfaces. Examination of the mixed-fluid interfaces as a function of concentration threshold, in the present data, showed that the c_1 threshold is above the noise level. The $c = c_1$

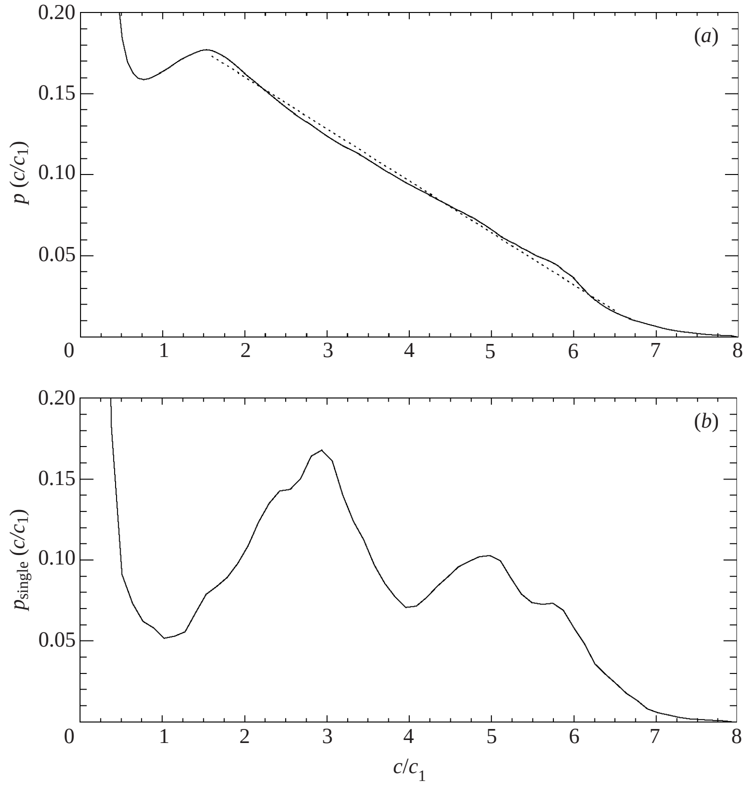

FIGURE 5. (*a*) Ensemble-averaged probability density function $p(c/c_1)$ of the concentration field for the three-dimensional space–time measurements, cf. figures 3 and 4. A linear fit for a range of concentration thresholds in the flow interior is also indicated (dotted line). (*b*) Concentration distribution $p_{\text{single}}(c/c_1)$ for an individual two-dimensional spatial image (figure 4*b*).

threshold also corresponds to the outer-interface concentration threshold employed in a study of two-dimensional spatial measurements at comparable flow conditions (Catrakis & Dimotakis 1996*a*, figure 8). Examination of the interfacial behaviour at higher concentration thresholds, corresponding to the interior of the flow, will be left for a future study.

Before exploring the connection between the concentration probability density function and the large-scale dynamics, it is interesting to consider again the interfacial interpretation of the probability density function from equation (3.1), in the light of the fact that, over a large range of concentration thresholds in the interior of the flow, this function appears to be linear for the present flow conditions. This linear behaviour, i.e.

$$p\left(\frac{c}{c_{\max}}\right) = \alpha\left(1 - \frac{c}{c_{\max}}\right) \quad \text{or} \quad p\left(\frac{c}{c_1}\right) = \beta - \gamma\frac{c}{c_1}, \tag{3.2}$$

is observed in the interior of the flow for mixed fluid over a wide range of concentration values, $c_1 \lesssim c \lesssim c_{\max}$, where $c_{\max}/c_1 \sim 7$ denotes the maximum concentration indicated for this linear dependence, with $p(c)\,\mathrm{d}c \equiv p(c/c_{\max})\,\mathrm{d}(c/c_{\max}) \equiv p(c/c_1)\,\mathrm{d}(c/c_1)$. Realizing that the ensemble-averaged space–time interfaces for the present flow will be axisymmetric with respect to the flow centreline, the average location of the c-fluid interfaces may be written in terms of the radial distance r from the flow centreline as $c = c(r)$, with its inverse relation $r = r(c)$. The probability density function can then be written using equation (3.1) in terms of the ensemble-averaged interfacial behaviour as

$$p(c) = \frac{1}{V_\delta}\left|\frac{\mathrm{d}}{\mathrm{d}c}\left[\frac{\pi r^2(c)}{\delta^2}V_\delta\right]\right|, \tag{3.3}$$

for $c_1 \leqslant c \leqslant c_0$, where the outer scale of the flow is denoted by δ as noted above. The observed linear concentration dependence of $p(c)$, expressed in equation (3.2), and relation (3.3) imply a linear concentration dependence for the radial location of the ensemble-averaged interfaces, i.e.

$$\frac{2r(c)}{\delta} = 1 - \frac{c}{c_{\max}} \quad \text{or} \quad \frac{c(r)}{c_{\max}} = 1 - \frac{2r}{\delta}, \tag{3.4}$$

over the range of internal thresholds. Combining equations (3.2)–(3.4), the dimensionless parameters α, β and γ in the linear dependence of the concentration probability density become

$$\alpha = \frac{\pi}{2}, \quad \beta = \alpha\frac{c_1}{c_{\max}}, \quad \gamma = \alpha\left(\frac{c_1}{c_{\max}}\right)^2. \tag{3.5}$$

It can be noted that the behaviour of the ensemble-averaged interfaces above the mixing transition, in the interior of this flow, corresponds to an average concentration field with uniform radial gradient of concentration.

The present linear behaviour is found in the ensemble-averaged probability density function of the concentration field, as shown in figure 5(*a*). Note that this is distinct from the probability density function corresponding to the ensemble-averaged concentration field. The latter statistic corresponds simply to the well-known mean-concentration profile. The difference is that the linear dependence in figure 5(*a*) refers to the interfacial behaviour corresponding to the ensemble average of the probability density function computed over the instantaneous concentration fields. Averaging after the probability density function is computed for each realization retains and reveals more information on the behaviour of the interfaces, such as the uniform concentration-field radial gradient found here for the average internal-mixing behaviour of the flow.

Figure 5(*b*) shows the concentration distribution $p_{\text{single}}(c/c_1)$ for an individual two-dimensional spatial field, cf. figure 4(*b*). This demonstrates that the concentration-field behaviour for the instantaneous spatial-field images can be quite different from the ensemble-average result, cf. figure 5(*a*). In particular, figures 5(*b*) and 4(*b*) indicate the presence of multiple large-scale well-mixed regions in the flow, i.e. regions of nearly uniform-concentration fluid. This is a manifestation of large-structure dynamics akin to the well-known shear-layer mixing behaviour (e.g. Brown & Roshko 1974). The large-scale well-mixed regions provide a further indication that the present mixing observations correspond to behaviour above the mixing transition.

The observed linear scalar-threshold dependence in the ensemble-averaged probability density function of concentration, cf. figure 5(*a*), further indicates that the present mixing behaviour is above the mixing transition. What is the mechanism that generates the linear behaviour in the ensemble-averaged probability density of concentration, in equation (3.2), or equivalently in the average interfacial behaviour in equation (3.4)? What is the role of large-scale well-mixed spatial regions in the flow, such as the regions evident in figures 4(*a, b*) and 5(*b*)?

Consider the turbulent mixing process as it evolves, in the context of the instantaneous distribution of the concentration field, cf. figure 5(*b*). Mixing converts higher-concentration fluid, originally issued from the jet nozzle in this case, to lower-concentration fluid, i.e. from right to left along the c-axis in figure 5(*b*). The large-scale dynamics in the jet can be axisymmetric or non-axisymmetric, e.g. helical (see, for example, Dimotakis *et al.* 1983; Yoda *et al.* 1994). Here an axisymmetric model is considered which can be extended to the other cases. Assuming that a large-scale well-mixed structure propagates downstream through a given similarity plane, the large-scale spatial extent $L(t)$ of the nearly uniform region of concentration in the similarity plane, associated with the large structure, can be expected to have a velocity $U_L(t)$ expressed as

$$U_L(t) \equiv \frac{\mathrm{d}L(t)}{\mathrm{d}t} \sim \frac{\delta}{L(t)} U_\mathrm{c}, \tag{3.6}$$

where U_c is the large-structure velocity, realizing that the downstream part of the well-mixed region is on the centreline in this model and the velocity on the centreline scales inversely with downstream distance for this flow. Equation (3.5) implies that the transverse extent $L(t)$ of the well-mixed region in the similarity plane scales as

$$L(t) \sim (\delta U_\mathrm{c} t)^{1/2}. \tag{3.7}$$

Time here is understood to be relative to the moment each large structure first meets the similarity plane, and $0 < t \leqslant \tau_\delta = \delta / U_\mathrm{c}$. Each well-mixed large-structure region will contribute a local peak in the probability density. In the $p(c)$ vs. c coordinates (figure 5*b*), each such peak propagates toward higher probability densities and lower concentration thresholds. The contribution, $p_L(c,t)$, of each well-mixed region to the concentration-field probability density can be expressed from geometrical considerations using the interfacial interpretation of the probability density, cf. equation (3.1), as

$$p_L(c,t) \sim \delta_D(c - c_L)\frac{L^2(t)}{\delta^2} \sim \delta_D(c - c_L)\frac{U_\mathrm{c}}{\delta} t, \tag{3.8}$$

where c_L denotes the concentration value corresponding to the nearly uniform well-mixed region and δ_D denotes the Dirac delta function. This result can be expected to hold also for multiple, i.e. nested, well-mixed regions, cf. figures 4(*b*) and 5(*b*). The contribution of each well-mixed region to the similarity-plane concentration probability density function may be expected therefore to increase linearly with time. As each large-structure propagates, the nearly uniform concentration value it generates can be considered in this model as decaying in time linearly, i.e.

$$\frac{c_L(t)}{c_{\max}} \sim 1 - \frac{U_\mathrm{c}}{\delta} t, \tag{3.9}$$

as indicated by the ramp-like concentration signals found in previous studies (e.g. Antonia *et al.* 1979; Sreenivasan, Antonia & Britz 1979). The linear temporal dependence in the large-structure contribution $p_L(c,t)$, in equation (3.8), and the linear temporal decay of concentration $c_L(t)$ in the large structure, imply the linear concentration dependence of the probability density observed here, cf. equation (3.2) and figure 5(*a*). This description also suggests that the departure from linearity in the concentration probability density in figure 5(*a*), at the low thresholds, arises from the dynamics of the finite number of nested large-scale structures. The above arguments indicate that the dynamics of the large-scale well-mixed regions in this flow can account for the linear $p(c)$ behaviour observed over a wide range of intermediate thresholds.

4. Dynamics of outer fluid interfaces

As discussed in § 1, of particular interest is the behaviour of the outer interface, i.e. the interface between mixed fluid and pure ambient fluid. From the three-dimensional space–time concentration-field data, isosurfaces of concentration were identified at the $c = c_1$ threshold which is in the vicinity of the local minimum in the concentration probability density, as described in § 3, cf. figure 5(*a*). An example of a two-dimensional space–time x, t outer interface is depicted in figure 6(*a*) superimposed on a grey-level visualization of the corresponding concentration field, cf. figure 4(*a*). Although the interface exhibits features over many scales, it has a greatly reduced extent of large-scale convolutions relative to the behaviour below the mixing transition, cf. figure 3 in Catrakis & Dimotakis (1996*a*). The absence of pronounced large-scale convolutions, evident in figure 6(*a*), was confirmed in numerous other two-dimensional space–time slices in the vicinity of the flow centreline and with otherwise random orientation. Similar behaviour was observed for the two-dimensional spatial x, y outer interfaces, an example of which is shown in figure 6(*b*). The present measurements show that the outer interfaces are dynamically confined primarily in the vicinity of the instantaneous large-scale boundaries of the flow. The visualizations in figure 6(*a, b*) support the conclusion from § 3, i.e. that mixing of pure fluid is initiated primarily in the vicinity of the unsteady large scales of the flow.

The present measurements enable a direct examination of the whole-field behaviour of the three-dimensional space–time outer interfaces. A transparent visualization of a three-dimensional outer interface is shown in figure 7. This visualization contains the flow centreline and was created from one of the present $\sim 1000^3$ data sets. Two-dimensional space–time slices of the outer interface, spanning the entire range of azimuthal orientations and containing the flow centreline, were identified and superimposed to produce the visualization shown in figure 7. Darker regions denote higher values of the probability density of the radial location of the interface, i.e. the distance from the flow centreline. Consistent with the observations in § 3, the dark regions in figure 7 are confined to a relatively narrow range of radial locations. The most striking feature is the large-scale gap spanning a wide range of radial locations in the interior of the flow, where the outer interface is seen to be absent throughout its temporal evolution. The features evident in the space–time visualization in figure 7 can also be interpreted as interfacial velocities. Near-vertical interfacial elements, in figure 7, correspond to low transverse velocities. Features inclined relative to the flow-centreline direction indicate higher transverse velocities. The interfacial features at locations of smaller radius exhibit a larger extent of transverse velocity fluctuations, reflecting the propagation of vortical structures through the interior region bounded by the outer interfaces.

A visualization of the whole-field dynamics of the outer interface viewed along the time axis is shown in figure 8. The outer interface identified from each of ~ 1000 temporally sequential spatial images was superimposed to create this visualization. Darker regions again denote higher values of the probability density of the radial location of the outer interface, cf. figure 7. Because this is a view in the time direction, darker regions also include the interfacial features with reduced transverse velocity fluctuations, i.e. at locations of larger radius. These are similar to the interfacial features that are seen as relatively light regions in the view normal to the time axis in figure 7. The visualization in figure 8 shows that there is a region of relatively large-scale transverse extent in the interior of the flow which is not visited by the outer interface. Similar behaviour was found in visualizations of all the current data

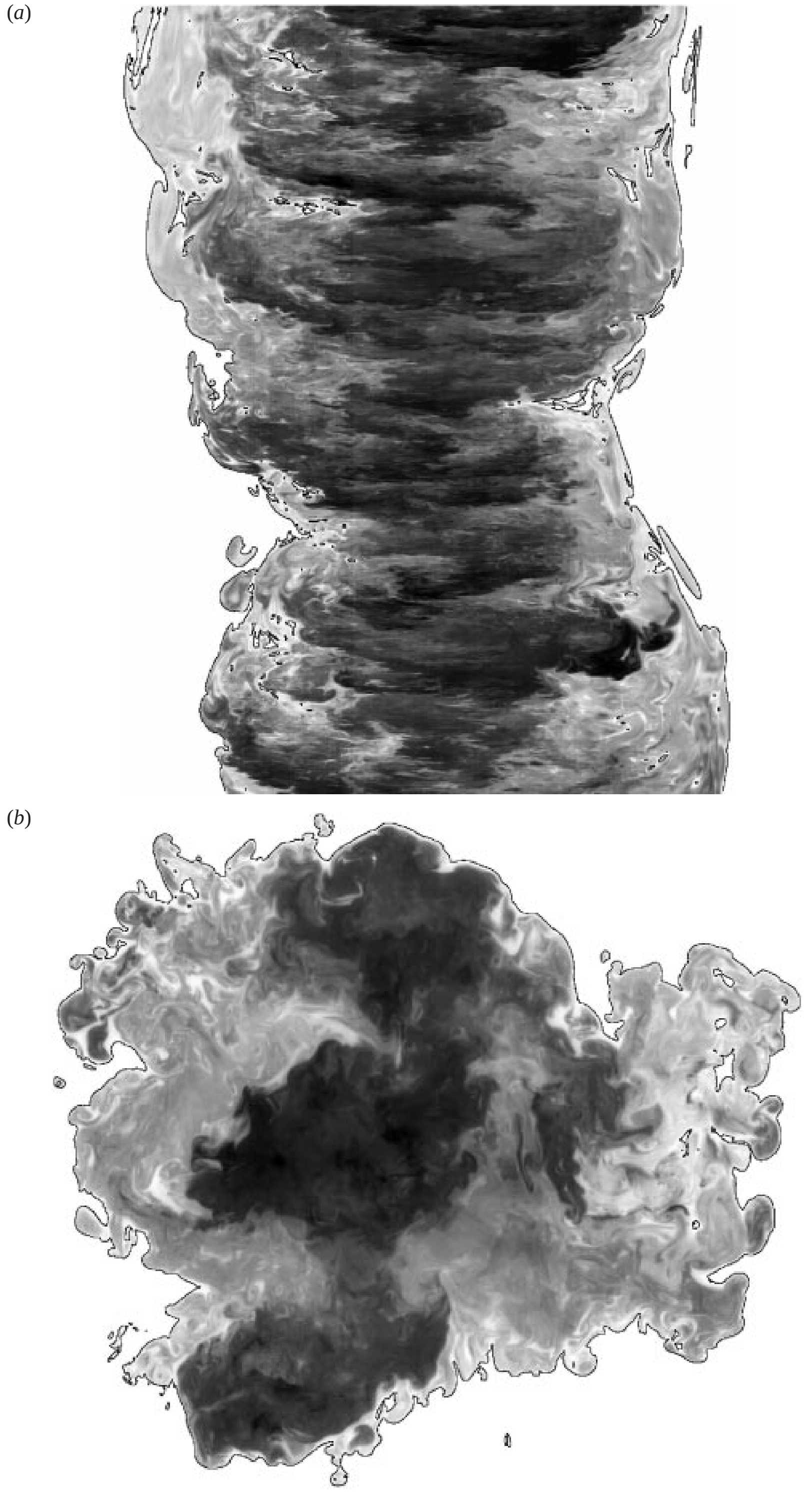

FIGURE 6. Outer interfaces derived from the three-dimensional space–time measurements and superimposed on the concentration field: (*a*) space–time x, t interface; (*b*) spatial x, y interface.

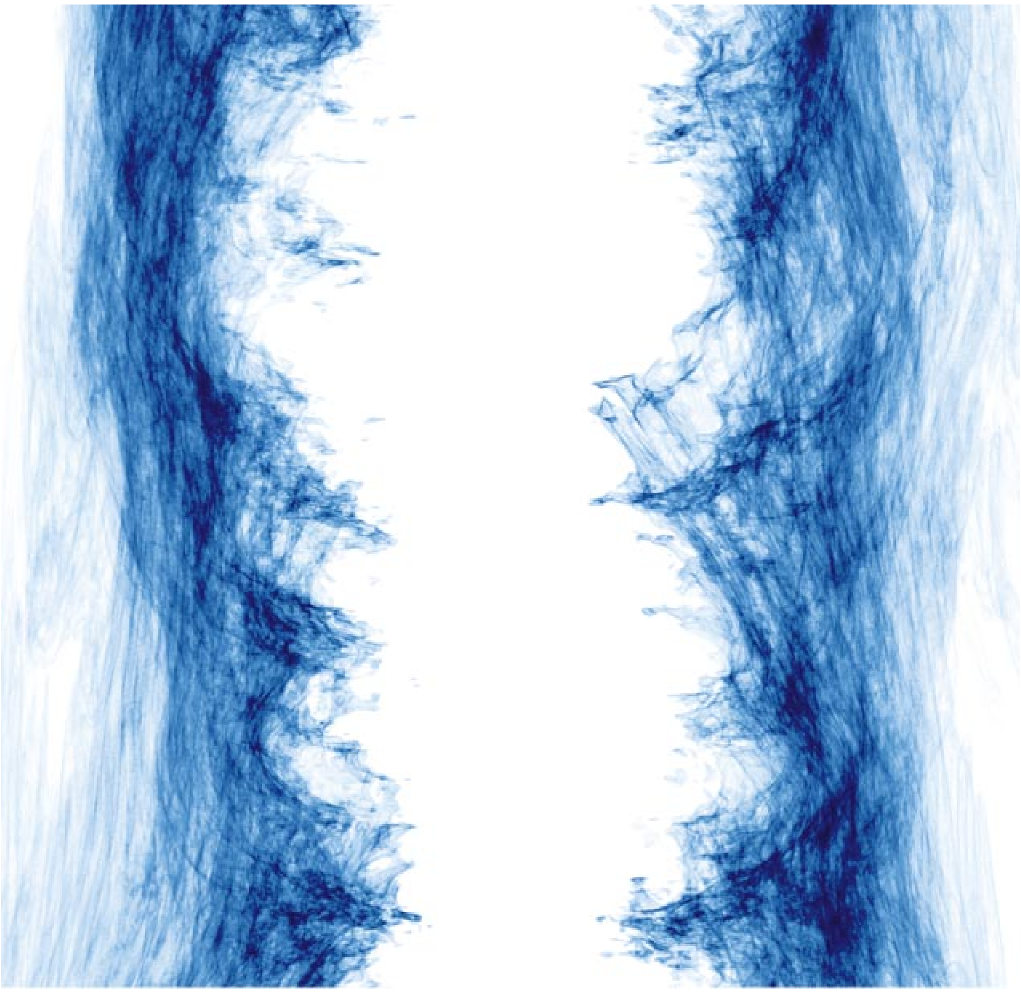

FIGURE 7. Whole-field transparent visualization of one of the $\sim 1000^3$ three-dimensional space–time outer interfaces viewed normal to the time axis and containing the flow centreline. Time increases vertically, cf. figures 3(a), 4(a) and 6(a). Darker regions indicate radial locations of higher probability density. The large-scale gap near the centre of the visualization shows the absence of the outer interface from a wide range of radial locations in the interior of the flow.

at the same flow conditions. This provides further support for the above observations that the dynamics of the flow result in outer interfaces that remain confined primarily near the instantaneous large scales.

What is the flow mechanism that results in the observed qualitatively different behaviour of the outer interfaces above the mixing transition? Entrainment of pure ambient fluid is known to be primarily accomplished by the large structures, both below and above the transition (e.g. Brown & Roshko 1974). The initiation of the entrainment process is not expected to change across the transition since, for example, the jet far-field growth rate is largely insensitive to the transition. The behaviour observed here that entrainment as well as mixing are initiated at the large scales must mean that this is due primarily to large-scale dynamics coupled with the emergence of small-scale structures inside large structures, generated as a result of internal instabilities, above the transition. As the large-scale structures entrain pure

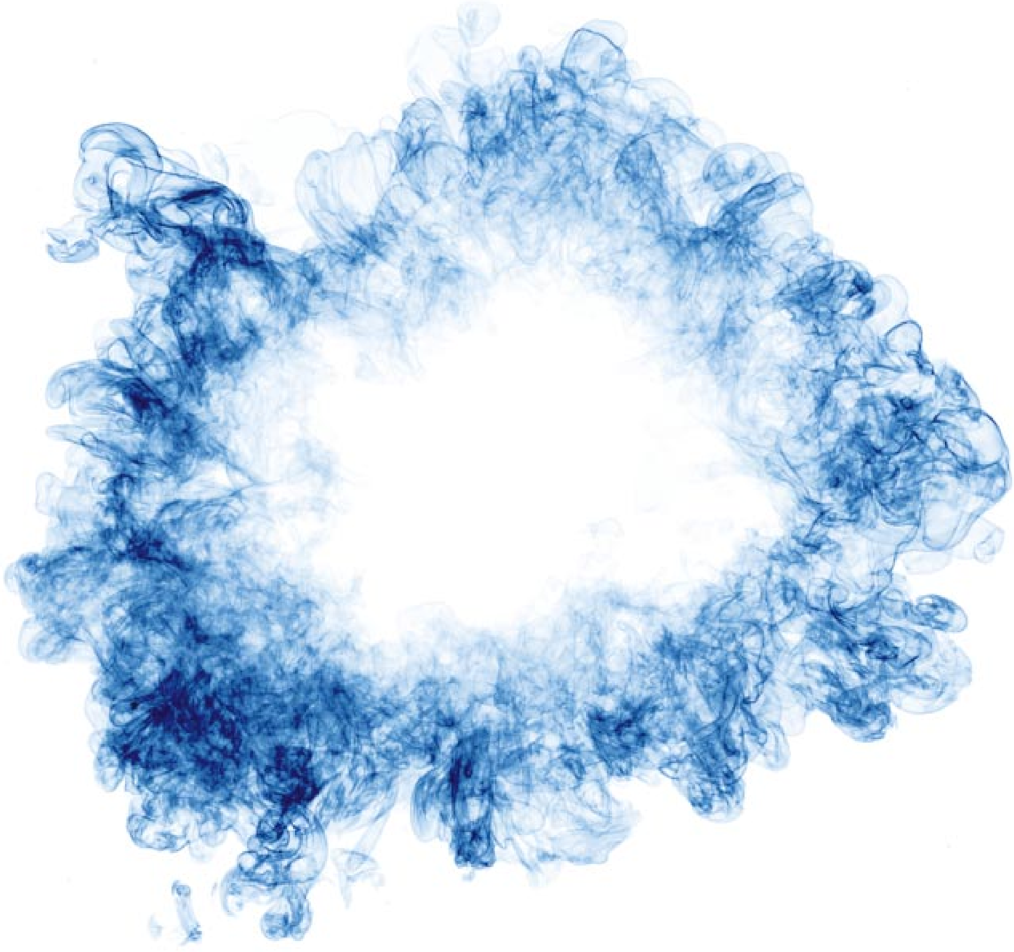

FIGURE 8. Visualization of the whole-field dynamics of a three-dimensional space–time outer interface derived from the present $\sim 1000^3$ measurements. This transparent view is along the time axis. Darker regions correspond to higher values of the probability density of radial location, i.e. distance from the flow centreline. A large-scale region in the interior of the flow, which is not visited by the outer interface, is again evident, cf. figure 7.

ambient fluid, the small-scale structures that are internal to the large structures, above the transition, initiate mixing of pure ambient fluid near the instantaneous large-scale boundaries of the flow. This results in outer interfaces dynamically confined primarily near the unsteady large scales, consistent with the observations in this work (figures 4*a*, 6*a*, 7 and 8).

As alluded to in § 1 and § 2, the dynamics of the outer interfaces can be expected to be crucial in the context of quantifying the mixing efficiency of the flow. Whereas identification of the extent to which the concentration field is homogenized requires knowledge of the behaviour of both the outer interfaces and internal interfaces, the total fraction of mixed fluid in the flow is determined entirely by the outer interfaces. Denoting by α_m the mixing efficiency, or fraction of mixed fluid, this may be written as

$$\alpha_m = \int_{c_1}^{c_{max}} p(c)\, dc, \tag{4.1}$$

Figure 9. Whole-field visualization of the outer-interfacial surface derived from the $\sim 1000^3$ three-dimensional space–time x, y, t measurements, cf. figures 7 and 8. This is an opaque view with time increasing vertically.

where the integration is carried out over mixed fluid only, i.e. excluding concentration values that correspond to pure ambient fluid or pure jet fluid. By definition, $0 < \alpha_m \leqslant 1$ for miscible fluids. While the probability density function $p(c)$ across the range of concentration values corresponding to mixed fluid involves the dynamics of all mixed-fluid interfaces, the mixing-efficiency integral in equation (4.1) is actually determined solely by the behaviour of the outer interfaces. This can be appreciated by noting that

$$\alpha_m = \frac{V_{outer}}{V_\delta}, \tag{4.2}$$

expressed here for constant-density flows, where V_{outer} is the volume of fluid enclosed by the outer interfaces, cf. equations (3.1) and (4.1). It is the volume enclosed by the outer interfaces, rather than the interfacial surface area, that determines the mixing efficiency.

The dynamics of the outer interfaces, therefore, governs the mixing efficiency. Figure 9 depicts a visualization of the space–time outer-interfacial surface. Large-scale dynamical features are evident. Realizing that the mixing efficiency is sensitive to

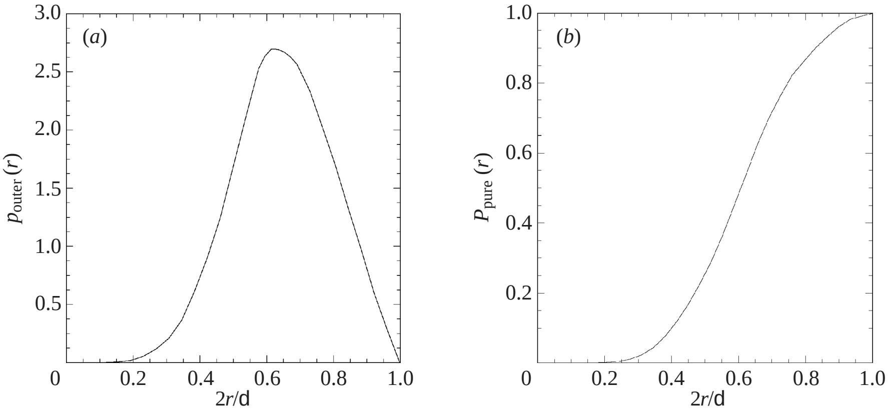

FIGURE 10. (*a*) xxxxEnsemble-averaged probability density $p_{\mathrm{outer}}(r)$ of the radial location of the outer interface from the flow centreline. (*b*) Ensemble-averaged probability $P_{\mathrm{pure}}(r)$ of pure ambient fluid as a function of radial distance from the flow centreline.

the volume enclosed by the outer interface rather than the surface area, cf. equations (4.1) and (4.2), it follows that it is the large-scale dynamics of the outer interface that provide the dominant contribution to the mixing efficiency. While the small-scale dynamics contributes greatly to the interfacial surface area (e.g. Catrakis *et al.* 2002), the mixing efficiency is most sensitive to the large-scale dynamics of the outer interface. Reduced variations in large-scale convolutions of the outer interface will generally result in a higher mixing efficiency, as noted above in the context of the mixing transition. Above the transition, such as for the present flow conditions, knowledge of the radial location of the outer interface is useful for examining high-Reynolds-number mixing-efficiency behaviour.

The ensemble-averaged probability density function $p_{\mathrm{outer}}(r)$ of the radial location of the outer interfaces from the flow centreline is shown in figure 10(*a*). This was computed from the three-dimensional space–time outer interfaces and is normalized such that

$$\int_0^{\delta/2} p_{\mathrm{outer}}(r)\,\mathrm{d}r = 1, \tag{4.3}$$

with $\delta/2$ the maximum radial location of the outer interface from the flow centreline. The probability density is seen to be precisely zero in the vicinity of the flow centreline, i.e. near $r = 0$, reflecting the present observations that no pure ambient fluid is able to enter and remain unmixed in that region of the flow, cf. figures 4(*a*, *b*), 6(*a*, *b*), 7 and 8. The largest probability density is found at a radial location $2r/\delta \sim 0.6$. The width of the probability density function $p_{\mathrm{outer}}(r)$ reflects, as expected, the unsteadiness of the outer interfaces and of the large-scale flow boundaries. To investigate this further, the fraction of pure fluid as a function of radial location should also be evaluated. The present whole-field measurements of the outer interfaces enable the examination of the variation of the fraction of pure fluid, relative to mixed fluid, in the flow.

The ensemble-averaged probability $P_{\mathrm{pure}}(r)$ of pure ambient fluid as a function of radius is shown in figure 10(*b*). By definition, $0 \leqslant P_{\mathrm{pure}}(r) \leqslant 1$ at all radial locations. The probability $P_{\mathrm{pure}}(r)$ is related directly to the mixing efficiency α_{m} as

$$\alpha_{\mathrm{m}} = 1 - \int_0^{\delta/2} P_{\mathrm{pure}}(r)\,\mathrm{d}r, \tag{4.4}$$

cf. equation (4.1) and figure 10(*b*). For the present measurements, the mixing efficiency is estimated to be $\alpha_m \sim 0.6$ which also agrees with the behaviour of $p(c)$, cf. figure 5(*a*) and equations (3.2) and (4.1). Consistent with the result in figure 10(*a*), the probability $P_{pure}(r)$ is identically zero near the flow centreline reflecting the absence of pure ambient fluid at those radial locations. In general, $P_{pure}(r) \neq \int_0^r p_{outer}(r')\,dr'$, because the probability density $p_{outer}(r)$ at a given radial location is sensitive to interfacial behaviour at other radial locations, cf. equation (4.3), whereas the probability $P_{pure}(r)$ is not. Figures 10(*a*) and 10(*b*) further indicate that the unsteadiness of the outer interfaces is primarily the result of the dynamics of the large-scale boundaries of the flow. That the largest contributions to the mixing efficiency are from the large-scale outer-interface dynamics is also indicated in figure 11(*a*, *b*) which visualizes the relative extent of pure vs. mixed fluid.

5. Distribution of interfacial scales

In this section, the distribution of interfacial scales will be computed for the whole-field three-dimensional space–time outer interfaces. The distribution of scales will be defined in terms of generalized level-crossing spacings. The statistics of level-crossing spacings have been examined in various flows in the past, following the pioneering studies of Liepmann (1949), e.g. on the basis of point measurements (e.g. Sreenivasan, Prabhu & Narasimha 1983) and two-dimensional measurements (e.g. Catrakis & Bond 2000). Such statistics provide information about the behaviour of the interfaces in physical space, as opposed for example to power spectra which are in Fourier space. A generalization of level-crossing spacings to analogous spacing scales for multi-dimensional interfaces has been developed (Catrakis 2000). This generalized framework will be applied to the present measurements of the three-dimensional space–time outer interfaces.

To compute the distribution of interfacial scales, box-counting techniques can be employed. A bounding box of size δ_b is identified and successively partitioned into smaller boxes each of size λ in order to count the number of boxes $N_3(\lambda)$ that cover the interface. Such quantities are called coverage functions (e.g. Sreenivasan 1991; Catrakis & Dimotakis 1996*a*). Care must be taken to avoid introducing artifacts of pixelization, of noise, or of the extent of the image field of view which have been shown previously to alter the apparent behaviour of the interfaces (e.g. Catrakis & Dimotakis 1996*a*, appendix). For this reason, the outer interfaces were represented in the present study using the boundary-outline method (Catrakis & Dimotakis 1996*a*) extended to three dimensions. For the present space–time x, y, t data, and for the purpose of investigating the distribution of interfacial scales, Taylor's hypothesis was applied utilizing the fact that the image framing rate in this study matched the mean speed of the outer interfaces, as discussed in § 2. In examining multi-dimensional data, there is a possibility of anisotropic behaviour. The coverage-function formalism has been extended so that it can be applied to anisotropic interfaces or other objects (e.g. Catrakis 2000). In general, it may be expected that there will be a distribution of directions associated with each scale. The focus of the present study, however, is not on anisotropy but on the scale distribution. The results below may be viewed in the context of averaging the behaviour, at each scale, over the distribution of interfacial directions.

For three-dimensional interfaces, the distribution of scales can be computed from the box-counting coverage fraction $F_3(\lambda)$ as

$$f_3(\lambda) = \frac{dF_3(\lambda)}{d\lambda}, \quad \text{where} \quad F_3(\lambda) = \left(\frac{\lambda}{\delta_b}\right)^3 N_3(\lambda), \tag{5.1}$$

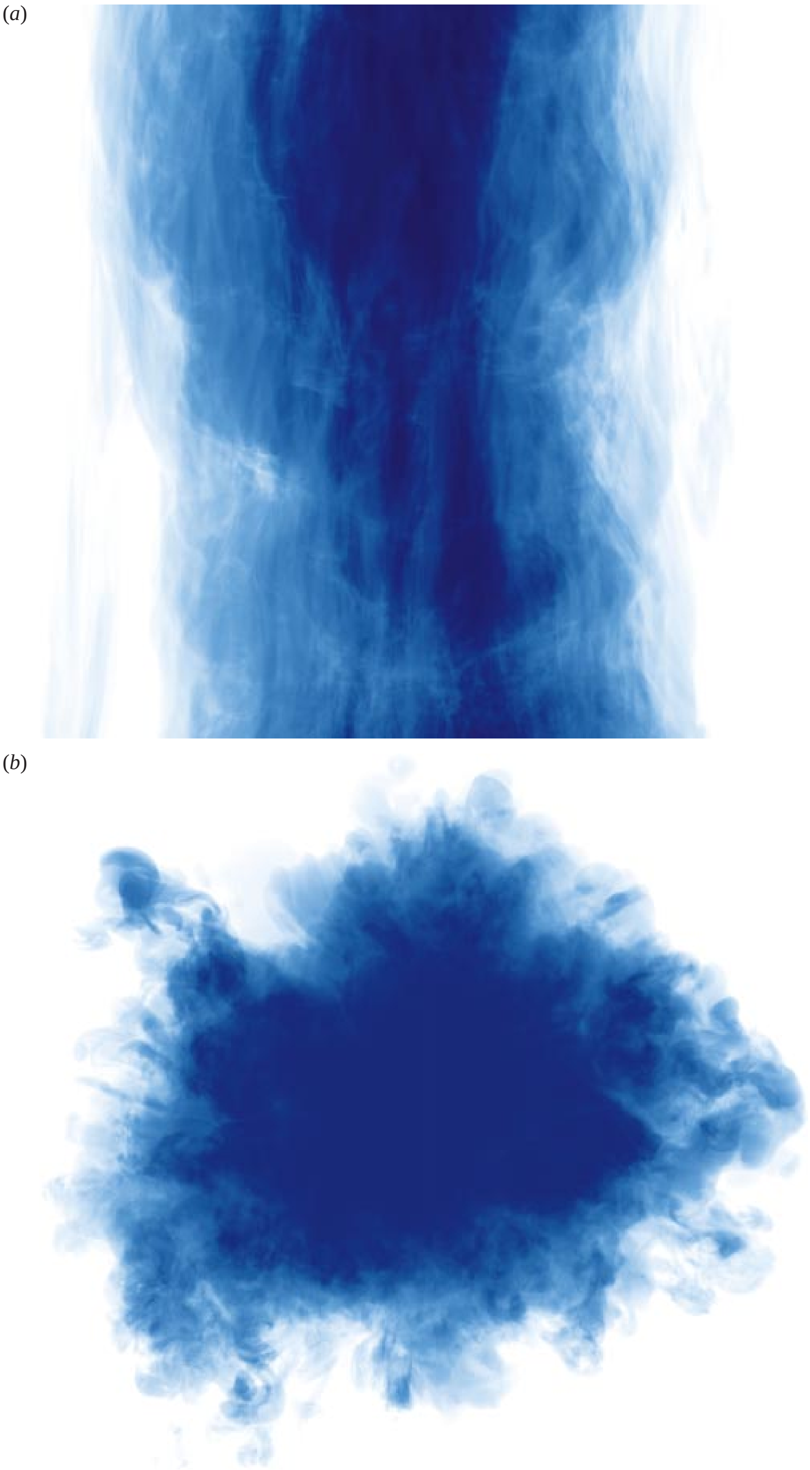

FIGURE 11. Visualizations of the relative extent of pure vs. mixed fluid in the flow, from the $\sim 1000^3$ measurements, illustrating the role of the outer-interface dynamics in the context of the mixing efficiency, cf. figure 10(*b*). All mixed fluid in the interior of the outer interfaces is labelled as blue, cf. figure 3(*a*, *b*). (*a*) View normal to the time axis. (*b*) View along the time axis.

and δ_b is the bounding-box size as noted above. The coverage fraction $F_3(\lambda)$ is the normalization of the coverage function by the total number of available λ-boxes at each stage of the bounding-box partitioning process. It is useful to view the coverage fraction as the geometric probability that a randomly selected λ-sized region in the flow, inside the bounding box, contains at least some part of the interface. The scale distribution $f_3(\lambda)$ is the probability density of the size of the largest box, randomly located within the bounding box, that does not contain any part of the interface. This provides the generalization of the notion of level-crossing spacings familiar from the study of one-dimensional signals, e.g. temperature or velocity-component traces. On the basis of point measurements, the statistics of level-crossing spacings have been examined in various fully developed turbulent flows (e.g. Sreenivasan *et al.* 1983) and in particular for concentration-field level crossings at Taylor Reynolds numbers as high as $Re_T \sim 5000$ in the atmospheric boundary layer (Yee *et al.* 1995). In addition to the studies of level-crossing behaviour, there have been various investigations of box-counting properties of interfaces (e.g. Sreenivasan & Meneveau 1986; Prasad & Sreenivasan 1990; Lane-Serff 1993; Catrakis & Dimotakis 1996*a*; Frederiksen *et al.* 1997). Box-counting properties can in fact be directly related to level-crossing statistics as was shown by Catrakis (2000). In three dimensions, for example, there is a one-to-one correspondence between the distribution of scales $f_3(\lambda)$ and the coverage dimension $D_3(\lambda)$. The latter is defined as the fractional decrease of the coverage function with increasing scale, i.e.

$$D_3(\lambda) \equiv -\frac{\mathrm{d}N_3(\lambda)/N_3(\lambda)}{\mathrm{d}\lambda/\lambda} \equiv -\frac{\mathrm{d}\log N_3(\lambda)}{\mathrm{d}\log\lambda}. \tag{5.2}$$

The coverage dimension is an important quantity because it provides a quantitative measure of the dimensionality of the interfaces. Relative to the topological dimension of the interfaces, the coverage dimension must be in the range

$$0 \leqslant D_3(\lambda) - 2 \leqslant 1 \tag{5.3}$$

for the present interfaces which are surfaces in three dimensions. The relation between the coverage dimension and the distribution of interfacial scales is

$$D_3(\lambda) = 3 - \frac{\lambda f_3(\lambda)}{\displaystyle\int_0^{\lambda} f_3(\lambda')\,\mathrm{d}\lambda'}, \tag{5.4}$$

as was derived for the general case by Catrakis (2000). This relation is invertible, i.e.

$$f_3(\lambda) = \frac{3 - D_3(\lambda)}{\lambda} \exp\left\{-\int_{\lambda}^{\delta_b} [3 - D_3(\lambda')]\frac{\mathrm{d}\lambda'}{\lambda'}\right\}. \tag{5.5}$$

Equations (5.4) and (5.5) constitute a transform pair in physical space that relates the dimensionality of the interfaces as a function of scale, across the entire range of scales, to the distribution of scales.

The ensemble-averaged coverage function, $N_3(\lambda)$, was computed by box counting for the three-dimensional x, y, t outer interfaces and the coverage dimension was determined using equation (5.2). Figure 12(*a*) shows the coverage dimension relative to the topological dimension of the interfaces, cf. equation (5.3). The ensemble-averaged bounding box size δ_b was employed to normalize the box scale as λ/δ_b. The uncertainty in the coverage dimension was estimated to be ±0.02 based on the fluctuations observed for the individual data sets. The continuous variation with

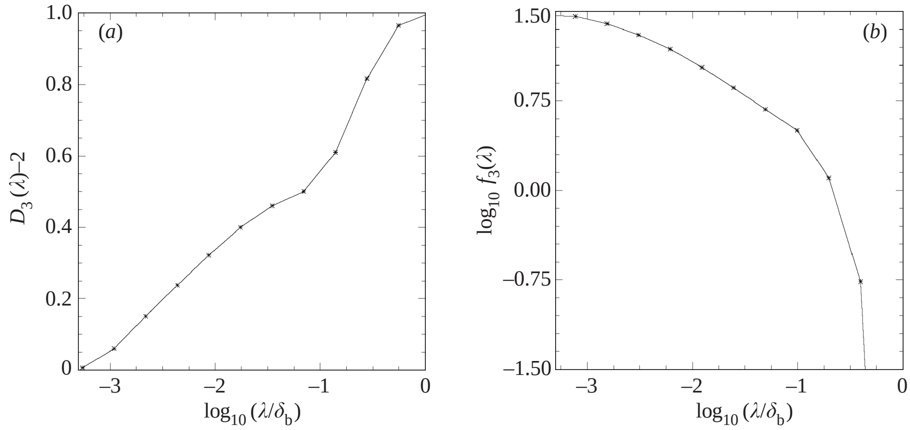

FIGURE 12. Ensemble-averaged behaviour of the three-dimensional space–time outer fluid interfaces throughout the range of scales. (*a*) Coverage dimension, $D_3(\lambda) - 2$, relative to the topological dimension of the interfaces as a function of scale (from figure 4*d* in Catrakis *et al.* 2002, shown here for completeness); (*b*) distribution of interfacial scales, $f_3(\lambda)$. The scale distribution corresponds to interfacial scales defined as generalized level-crossing spacings.

scale, evident in figure 12(*a*), indicates scale-dependent behaviour. Such behaviour corresponds to cumulative interfacial properties as was recently demonstrated by Catrakis *et al.* (2002). In interpreting the behaviour of the coverage function, and its relation to the interfacial dynamics, it is useful to appreciate that the coverage function $N_3(\lambda)$ essentially filters out interfacial information below the scale λ, i.e. the coverage function is sensitive primarily to interfacial features of size greater than or equal to λ. As a function of the scale λ, the coverage function is a cumulative quantity and therefore sensitive to all interfacial features above that scale. The coverage dimension is also a cumulative quantity because it integrates information across a range of scales, cf. equation (5.5).

The behaviour of the coverage dimension in figure 12(*a*) illustrates, therefore, the cumulative dynamics of the interfaces throughout the range of scales. The expected bounding values are confirmed in the behaviour of the present data, cf. equation (5.3). Away from the smallest scales, the coverage dimension is seen to depart from the topological dimension, consistent with visual observations, e.g. the visualization in figure 9. As the scale λ increases relative to the smallest scales, the coverage dimension departs continuously from the topological dimension, indicating that the interfaces become progressively more convoluted with increasing scale. This reflects the increasing range of scales that influence the behaviour of the coverage function and the coverage dimension. Figure 12(*b*) depicts the distribution $f_3(\lambda)$ of interfacial scales for the present measurements. It is seen that $f_3(\lambda)$ decreases continuously with increasing scale. The probability density of interfacial spacings is larger at the smaller scales, reflecting the fact that there are more small-scale empty boxes, i.e. regions that do not contain the interface. This behaviour is consistent with previous investigations of interfaces derived from lower-dimensional measurements of interfaces (e.g. Catrakis & Dimotakis 1996*a*, *b*).

The present results indicate that the scale-cumulative behaviour of the interfaces across the range of scales can be scale dependent above the mixing transition. This is not inconsistent with the classical self-similarity ideas of Richardson (1922) and Taylor (1935), as may be appreciated by the following argument. The complexity of the dynamics of the interfaces, at a given scale, is primarily influenced by flow structures at or below that scale. Examination of the interface at increasing scales can be expected therefore to show progressively more convoluted behaviour, because of the larger range of scales subtended. Examination of interfacial self-similarity requires scale-local measures that can quantify the interfacial behaviour as a function of scale. Such scale-local measures were recently introduced in the context of area–volume properties of interfaces and indicate the presence of self-similarity in the scale-local behaviour coexisting with scale dependence in the cumulative properties that arises from large-scale effects (Catrakis *et al.* 2002). As discussed in §4, while it is the interfacial behaviour across the entire range of scales that determines the mixing efficiency, the dominant contribution is from the large-scale features of the outer interfaces.

6. Conclusions

The experiments conducted in this study have provided $\sim 1000^3$ whole-field three-dimensional space–time measurements above the mixing transition, at a Reynolds number of $Re \sim 20\,000$ and Schmidt number of $Sc \sim 2000$ in turbulent jets at a far-field distance of $z/d \sim 500$ nozzle diameters. These measurements have resolved the entire range of scales of the outer interfaces in fully developed turbulence in three out of the four space–time dimensions. The outer interfaces are the interfaces between mixed fluid and pure ambient fluid and are physically important for understanding turbulent mixing. The present measurements have enabled a direct examination of the large-scale behaviour of the outer interfaces including both the temporal dynamics and spatial structure. Investigations of the whole-field mixing behaviour and dynamics of the outer interfaces above the mixing transition are particularly important because the properties of the fluid interfaces in such flows can be expected to be representative, at least qualitatively, of the mixing behaviour in high-Reynolds-number flows in general.

The principal finding in this work is that the outer interfaces above the mixing transition are dynamically confined primarily near the instantaneous large-scale boundaries of the flow. Molecular mixing of pure ambient fluid is initiated in the vicinity of the unsteady large scales. These observations are quantified in terms of the probability density of the location of the outer interfaces relative to the flow centreline and the probability of pure ambient fluid as a function of distance from the centreline. The present findings show that the turbulent mixing behaviour above the mixing transition is qualitatively different from the known behaviour below the transition where pure ambient fluid can penetrate deeply into the interior of the flow as unmixed fluid. The direct examination of the whole-field dynamics of the outer interfaces, demonstrated in the present experiments, makes it possible to identify the mechanism by which mixing of pure ambient fluid is initiated in the flow. The present observation that the outer interfaces are dynamically found near the instantaneous large-scale boundaries of the flow can be explained by considerations of large-scale entrainment, above the mixing transition, whereby the large-scale flow dynamics coupled with the emergence of small-scale structures internal to the large structures initiate mixing near the unsteady large scales. Because large-scale dynamics is prevalent in turbulent shear flows (e.g. Roshko 1992), this turbulent mixing mechanism may be expected, at least qualitatively, in other flows at high Reynolds numbers, i.e. above the mixing transition, with the large-scale behaviour of the outer interfaces governed by the large-scale vortex dynamics.

Visualizations of the whole-field mixing behaviour from the present measurements show multiple large-scale regions of spatially nearly uniform-concentration fluid, i.e.

well-mixed fluid, in agreement with previous results above the mixing transition. A linear behaviour is found for the ensemble-averaged probability density function of concentration over a wide range of concentration values in the interior of this flow. This finding can be accounted for in terms of the dynamics of large-scale well-mixed regions. The linear dependence in the concentration probability density function corresponds to mixing behaviour above the mixing transition. This provides a quantitative means to extrapolate the ensemble-averaged mixing behaviour to higher Reynolds numbers.

The dynamics and structure of the outer interfaces determine the mixing efficiency of the flow, i.e. fraction of mixed fluid. The behaviour of the outer interfaces across the entire range of scales can be quantified in terms of the distribution of interfacial scales. While the dynamics and structure of the outer interfaces across the whole range of scales determine the mixing efficiency, it is the large-scale dynamics of the outer interfaces that provides the dominant contribution. This suggests a new approach for developing predictive descriptions of the mixing efficiency in high-Reynolds-number turbulent flows.

This work is supported by the National Science Foundation through Career Award Grant CTS-9875036 (Dr C. Chen and Dr J. Foss, Program Managers) and by the Air Force Office of Scientific Research through Grant F49620-02-1-0142 (Dr T. Beutner, Program Manager), and is part of a long-range research program on high-Reynolds-number turbulent flows and fluid interfaces. The authors are grateful to the referees for their insightful comments.

REFERENCES

Adrian, R. J., Meinhart, C. D. & Tomkins, C. D. 2000 Vortex organization in the outer region of the turbulent boundary layer. *J. Fluid Mech.* **422**, 1–54.

Antonia, R. A., Chambers, A. J., Friehe, C. A. & Van Atta, C. W. 1979 Temperature ramps in the atmospheric surface layer. *J. Atmos. Sci.* **36**, 99–108.

Brown, G. L. & Roshko, A. 1974 On density effects and large scale structure in turbulent mixing layers. *J. Fluid Mech.* **64**, 775–816.

Catrakis, H. J. 2000 Distribution of scales in turbulence. *Phys. Rev.* E **62**, 564–578.

Catrakis, H. J., Aguirre, R. C. & Ruiz-Plancarte, J. 2002 Area–volume properties of fluid interfaces in turbulence: scale-local self-similarity and cumulative scale dependence. *J. Fluid Mech.* **462**, 245–254.

Catrakis, H. J. & Bond, C. L. 2000 Scale distributions of fluid interfaces in turbulence. *Phys. Fluids* **12**, 2295–2301.

Catrakis, H. J. & Dimotakis, P. E. 1996*a* Mixing in turbulent jets: scalar measures and isosurface geometry. *J. Fluid Mech.* **317**, 369–406.

Catrakis, H. J. & Dimotakis, P. E. 1996*b* Scale distributions and fractal dimensions in turbulence. *Phys. Rev. Lett.* **77**, 3795–3798.

Catrakis, H. J. & Dimotakis, P. E. 1998 Shape complexity in turbulence. *Phys. Rev. Lett.* **80**, 968–971.

Dahm, W. J. A. & Dimotakis, P. E. 1990 Mixing at large Schmidt number in the self-similar far field of turbulent jets. *J. Fluid Mech.* **217**, 299–330.

Dalziel, S. B., Linden, P. F. & Youngs, D. L. 1999 Self-similarity and internal structure of turbulence induced by Rayleigh–Taylor instability. *J. Fluid Mech.* **399**, 1–48.

Dimotakis, P. E. 1991 Turbulent free shear layer mixing and combustion. In *High Speed Flight Propulsion Systems* (ed. S. Murthy & E. Curan). Progress in Astronautics and Aeronautics, vol. 137. AIAA.

Dimotakis, P. E. 2000 The mixing transition in turbulent flows. *J. Fluid Mech.* **409**, 69–98.

Dimotakis, P. E., Catrakis, H. J. & Fourguette, D. C. L. 2001 Flow structure and optical beam propagation in high-Reynolds-number gas-phase shear layers and jets. *J. Fluid Mech.* **433**, 105–134.

Dimotakis, P. E., Miake-Lye, R. C. & Papantoniou, D. A. 1983 Structure and dynamics of round turbulent jets. *Phys. Fluids* **26**, 3185–3192.

Frederiksen, R. D., Dahm, W. J. A. & Dowling, D. R. 1997 Experimental assessment of fractal scale similarity in turbulent flows. Part 2: Higher-dimensional intersections and non-fractal inclusions. *J. Fluid Mech.* **338**, 89–126.

Gad-el-Hak, M. 2000 *Flow Control: Passive, Active, and Reactive Flow Management.* Cambridge University Press.

Jumper, E. J. & Fitzgerald, E. J. 2001 Recent advances in aerooptics. *Prog. Aerospace Sci.* **37**, 299–339.

Lane-Serff, G. F. 1993 Investigation of the fractal structure of jets and plumes. *J. Fluid Mech.* **249**, 521–534.

Liepmann, H. W. 1949 Die Anwendung eines Satzes über die Nullstellen Stochastischer Funktionen auf Turbulenzmessungen. *Helv. Phys. Acta* **22**, 119–126.

Liepmann, H. W. 1979 The rise and fall of ideas in turbulence. *Am. Sci.* **67**, 221–228.

Pope, S. B. 1988 The evolution of surfaces in turbulence. *Intl J. Engng Sci.* **26**, 445–469.

Prasad, R. R. & Sreenivasan, K. R. 1990 Quantitative three-dimensional imaging and the structure of passive scalar fields in fully turbulent flows. *J. Fluid Mech.* **216**, 1–34.

Richardson, L. F. 1922 *Weather Prediction by Numerical Process.* Cambridge University Press.

Roshko, A. 1976 Structure of turbulent shear flows: a new look. *AIAA J.* **14**, 1349–1357.

Roshko, A. 1991 The mixing transition in free shear flows. In *The Global Geometry of Turbulence* (ed. J. Jiménez), pp. 3–11. Plenum.

Roshko, A. 1992 Instability and turbulence in shear flows. In *Proceedings of the XVIIIth International Congress of Theoretical and Applied Mechanics, Haifa, Israel, August 22–28* (ed. S. R. Bodner, J. Singer, A. Solan & Z. Hashin). Elsevier.

Smits, A. J. & Dussauge, J.-P. 1996 *Turbulent Shear Layers in Supersonic Flow.* AIP Press.

Sreenivasan, K. R. 1991 Fractals and multifractals in fluid turbulence. *Annu. Rev. Fluid. Mech.* **23**, 539–600.

Sreenivasan, K. R., Antonia, R. A. & Britz, D. 1979 Local isotropy and large structures in a heated turbulent jet. *J. Fluid Mech.* **94**, 745–775.

Sreenivasan, K. R. & Meneveau, C. 1986 The fractal facets of turbulence. *J. Fluid Mech.* **173**, 357–386.

Sreenivasan, K. R., Prabhu, A. & Narasimha, R. 1983 Zero-crossings in turbulent signals. *J. Fluid Mech.* **137**, 251–272.

Taylor, G. I. 1935 Statistical theory of turbulence. Parts i–iv. *Proc. R. Soc. Lond.* A **151**, 421–478.

Vassilicos, J. C. & Hunt, J. C. R. 1991 Fractal dimensions and spectra of interfaces with application to turbulence. *Proc. R. Soc. Lond.* A **435**, 505–534.

Villermaux, E. & Innocenti, C. 1999 On the geometry of turbulent mixing. *J. Fluid Mech.* **393**, 123–147.

Yee, E., Chan, R., Kosteniuk, P. R., Chandler, G. M., Biltoft, C. A. & Bowers, J. F. 1995 Measurements of level-crossing statistics of concentration fluctuations in plumes dispersing in the atmospheric surface layer. *Boundary-Layer Met.* **73**, 53–90.

Yoda, M., Hesselink, L. & Mungal, M. G. 1994 Instantaneous three-dimensional concentration measurements in the self-similar region of a round high-Schmidt-number jet. *J. Fluid Mech.* **279**, 313–350.